SCIENTIFIC REPORTS

OPEN

NiCo nanoalloy encapsulated in graphene layers for improving hydrogen storage properties of $LiAlH_4$

Received: 13 January 2016
Accepted: 18 May 2016
Published: 07 June 2016

Chengli Jiao[1,2,3], Lixian Sun[2], Fen Xu[2], Shu-Sheng Liu[4], Jian Zhang[3], Xia Jiang[3] & Lini Yang[5]

NiCo nanoalloy (4–6 nm) encapsulated in grapheme layers (NiCo@G) has been prepared by thermolysis of a 3D bimetallic complex $CoCo[Ni(EDTA)]_2{\cdot}4H_2O$ and successfully employed as a catalyst to improve the dehydrogenation performances of $LiAlH_4$ by solid ball-milling. NiCo@G presents a superior catalytic effect on the dehydrogenation of $LiAlH_4$. For $LiAlH_4$ doped with 1 wt% NiCo@G ($LiAlH_4$-1 wt% NiCo@G), the onset dehydrogenation temperature of $LiAlH_4$ is as low as 43 °C, which is 109 °C lower than that of pristine $LiAlH_4$. 7.3 wt% of hydrogen can be released from $LiAlH_4$-1 wt% NiCo@G at 150 °C within 60 min. The activation energies of $LiAlH_4$ dehydrogenation are extremely reduced by 1 wt% NiCo@G doping.

Hydrogen storage is one of the most critical issues for fuel cell vehicular applications. Solid hydrogen storage materials such as carbon materials, MOFs, metal hydrides and complex hydrides have received significant attention as the safest and most effective storage media[1–10]. Among them, lithium alanate ($LiAlH_4$) is considered as one of the most promising hydrogen storage materials due to its high hydrogen storage capacity of 10.5 wt%. In the last two decades, $LiAlH_4$ has received particular attention aiming at reducing the operation temperature to meet the DOE criteria because it can release a total amount of 7.9 wt% of hydrogen in two steps (eqs 1 and 2) below a relatively low temperature, e.g. 220 °C.

$$3LiAlH_4 \rightarrow Li_3AlH_6 + 2Al + 3H_2 (5.3\ wt\%\ H_2,\ 150–175\,^{\circ}C) \quad (1)$$

$$Li_3AlH_6 \rightarrow 3LiH + Al + 3/2H_2 (2.6\ wt\%\ H_2,\ 180–220\,^{\circ}C) \quad (2)$$

Different methods have been explored for decrease of the dehydrogenation temperature of $LiAlH_4$, including particle size reduction by ball milling[11], synthesis of multi-hydride composites[12], and doping with catalysts[13,14]. Among these methods, doping with catalysts is considered as an effective approach for the dehydrogenation of $LiAlH_4$. Various catalysts have been investigated, such as Ti, Fe, Ni, V, Al, Al_3Ti, TiF_3, $TiCl_4$, $TiCl_3$, $NiCl_2$, VCl_3, $AlCl_3$, $FeCl_3$, $TiCl_3{\cdot}1/3AlCl_3$, TiH_2, $NiFe_2O_4$, carbon nanotube and so on[15–19]. Ni based catalysts have been widely explored. Zheng *et al.*[20] doped $LiAlH_4$ with Ni to reduce the temperature of the first dehydrogenation step by approximately 10–15 °C, with a great expense of the hydrogen storage capacity. Yuan *et al.*[21] prepared 2 mol% $NiCo_2O_4$ nanorod doped $LiAlH_4$, which can release 6.47 wt% of hydrogen at 150 °C within 150 min. Nevertheless, most of the systems present the disadvantage of loss of the overall hydrogen storage capacity, due to either a hydrogen release during the ball milling process or the large additional weight of the catalysts. Thus, it is desirable to develop an effective catalyst for the dehydrogenation of $LiAlH_4$.

[1]Key Laboratory of Biobased Materials, Qingdao Institute of Bioenergy and Bioprocess Technology, Chinese Academy of Sciences, No. 189 Songling Road, Qingdao 266101, P. R. China. [2]Guangxi Key Laboratory of Information Materials & Guangxi Collaborative Innovation Center of Structure and Property for New Energy and Materials, School of Material Science and Engineering, Guilin University of Electronic Technology, Guilin 541004, P. R. China. [3]Dalian Institute of Chemical Physics, Chinese Academy of Sciences, 457 Zhongshan Road, Dalian 116023, P. R. China. [4]INAMORI Frontier Research Center, Kyushu University, Nishi-ku, Fukuoka 8190395, Japan. [5]College of Chemistry, Liaoning University, Shenyang 110036, P. R. China. Correspondence and requests for materials should be addressed to L.S. (email: sunlx@guet.edu.cn) or F.X. (email: xufen@guet.edu.cn)

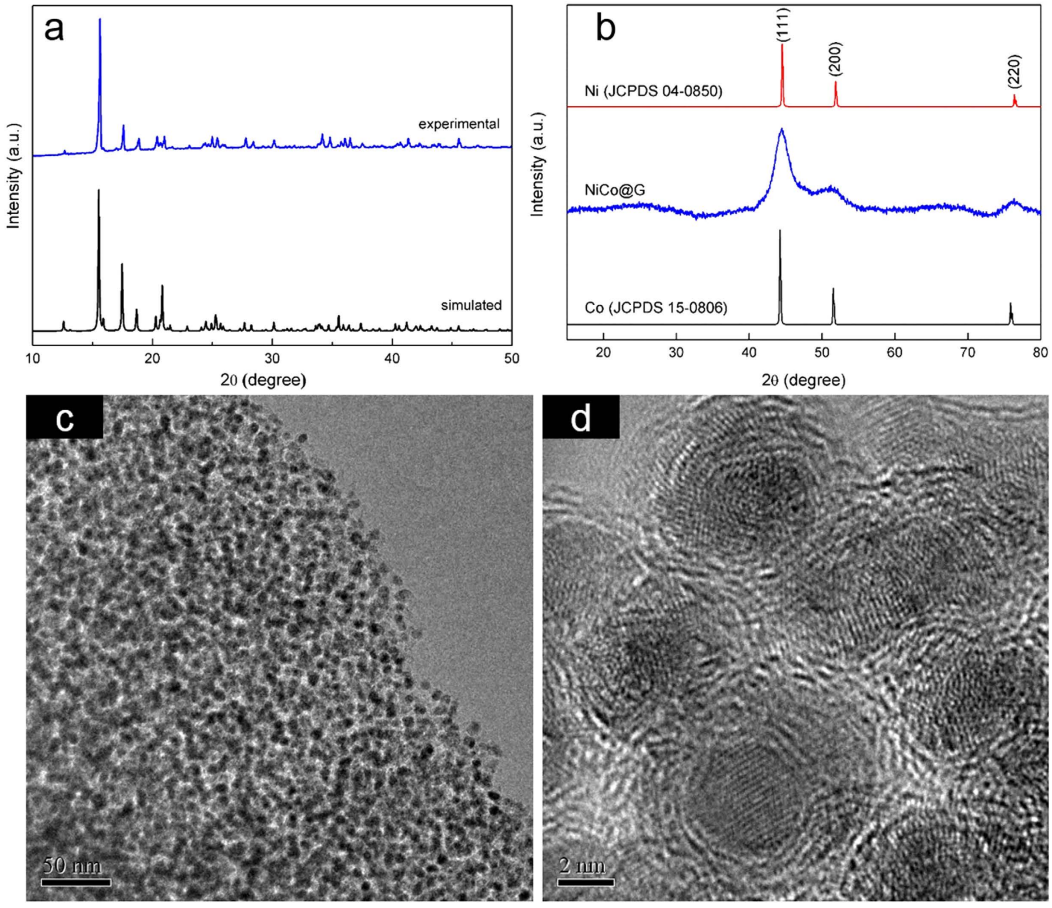

Figure 1. (**a**) XRD patterns of $CoCo[Ni(EDTA)]_2{\cdot}4H_2O$: simulated pattern on the basis of the single crystal structure according to the already published paper[30], and experimental pattern of $CoCo[Ni(EDTA)]_2{\cdot}4H_2O$ synthesized in this study; (**b**) XRD patterns of NiCo@G, fcc Ni (JCPDS card no. 04–0850) and fcc Co (JCPDS card no. 15–0806); TEM images of NiCo@G at different magnifications: (**c**,**d**).

Recently, metal/carbon composites has been developed for the dehydrogenation of $LiAlH_4$, including Co-decorated MWCNTs[22], Co@C[23], and Ni-containing mesoporous carbon scaffold (Ni-MCS)[24]. In the last two decades, bimetallic nanoparticles have received great interest for catalysis and electrocatalysis, due to their higher activity and selectivity than monometallic nanoparticles as a result of "synergistic effects"[25–28]. In addition, graphene more effectively improves the dehydrogenation behavior of $LiAlH_4$ than C_{60}, carbon nanotubes, and graphite[29]. In this study, we used NiCo nano alloy encapsulated in graphene layers (NiCo@G) as a catalyst and investigated the effects of NiCo@G on the dehydrogenation behavior of $LiAlH_4$. Preliminary results showed that excellent dehydrogenation properties of $LiAlH_4$ were achieved by 1 wt% NiCo@G doping.

Results and Discussion

Preparation and characterization of NiCo@G. Briefly, a 3D bimetallic complex $CoCo[Ni(EDTA)]_2{\cdot}4H_2O$, a precursor for NiCo@G, was firstly synthesized through solvothermal method. $CoCo[Ni(EDTA)]_2{\cdot}4H_2O$ precursor was thermally decomposed to NiCo@G as the final product at 500 °C in an argon flow. The Powder X-ray diffraction peaks (Fig. 1a) of the as-synthesized precursor $CoCo[Ni(EDTA)]_2{\cdot}4H_2O$ match well with the simulated pattern on the basis of the single crystal structure reported by Sapiña *et al.* (Supplementary Fig. S1)[30]. The Ni/Co molar ratio in NiCo@G is 1:1 as that in the precursor complex, which is confirmed by SEM-EDS data (Supplementary Fig. S2). As shown in Fig. 1b, the XRD pattern of NiCo@G shows peaks at $2\theta = 44.48$, 51.69 and 76.25°, matching those reported for (111), (200) and (220) planes of $Ni_{50}Co_{50}$ alloy with a fcc structure[31,32]. Their positions are slightly higher than those of pure fcc Co (44.22, 51.52 and 75.86°) and slightly lower than those of pure fcc Ni (44.51, 51.85 and 76.37°). Broadness of the characteristic diffraction peaks for NiCo alloy is due to the formation of nanosized NiCo particles. Furthermore, the characteristic reflections corresponding to hexagonal close packed (hcp) metallic Co can not be observed. The broad peak around $2\theta = 26°$ is the characteristic reflection for carbon. X-ray photoelectron spectroscopy (XPS) was used to examine the species present in the particles. The spectra of Ni 2p and Co 2p energy ranges were recorded (Supplementary Fig. S3). The positions of the 2p peaks are respectively 852.8 and 870.1 eV for Ni 2p, 778.3 and 793.3 eV for Co 2p, demonstrating Ni and Co in their zero-valent states[33–35]. TEM images are shown in Fig. 1c,d, indicating that the NiCo nanoalloy is encapsulated in multilayered graphene shells (NiCo@G). The NiCo nanoalloy are spherical in shape, with a highly

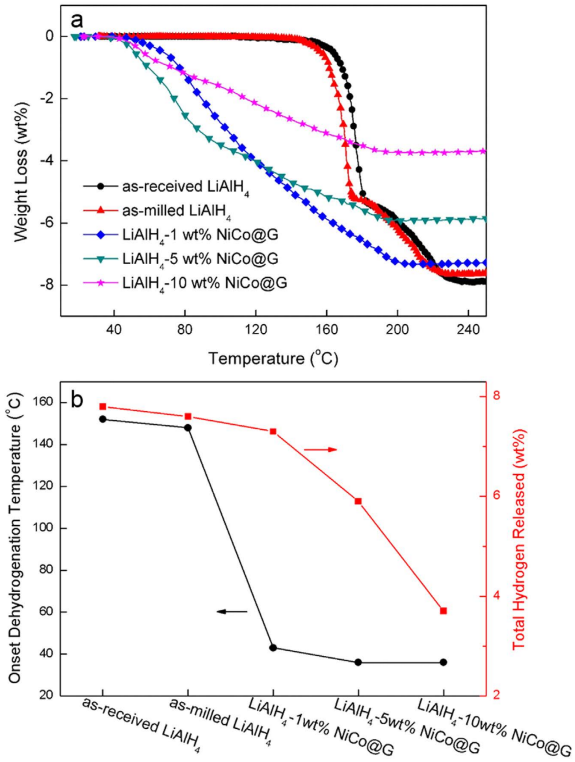

Figure 2. (**a**) Non-isothermal dehydrogenation curves (2 °C min^{-1}); (**b**) Onset dehydrogenation temperature and amount of total hydrogen released of as-received $LiAlH_4$, as-milled $LiAlH_4$ and $LiAlH_4$ doped with 1 wt%, 5 wt% and 10 wt% NiCo@G.

uniform size distribution ranging from 4 nm to 6 nm. In addition, the STEM corresponding element mapping (Supplementary Fig. S4) of NiCo@G confirms a homogeneous distribution of NiCo alloy over the sample.

Dehydrogenation performances. Figure 2a as shows the non-isothermal dehydrogenation performances of as-received $LiAlH_4$, as-milled $LiAlH_4$, and $LiAlH_4$ doped with 1 wt%, 5 wt% and 10 wt% NiCo@G. Compared to as-received $LiAlH_4$, as-milled $LiAlH_4$ exhibits a similar dehydrogenation behavior. The as-received $LiAlH_4$ starts to decompose at 152 °C, while the as-milled $LiAlH_4$ exhibits a slight decrease of 4 °C. It is obvious that addition of NiCo@G extremely improves the onset dehydrogenation temperature of $LiAlH_4$. The onset dehydrogenation temperature and the amount of hydrogen released of all samples are shown in Fig. 2b. The onset desorption temperature decreases with the increasing NiCo@G percent. $LiAlH_4$-1 wt% NiCo@G starts to decompose at 43 °C, which is 109 °C lower than as-received $LiAlH_4$. For 5 wt% and 10 wt% NiCo@G doped samples, the onset dehydrogenation temperature is as low as 36 °C, which is 116 °C lower than as-received $LiAlH_4$. However, raising the NiCo@G percent results in a decrease of the amount of hydrogen released. Only 5.9 wt% and 3.7 wt% of hydrogen are respectively released for $LiAlH_4$-5 wt% NiCo@G and $LiAlH_4$-10 wt% NiCo@G, due to the increasing catalyst percent and the premature dehydrogenation during the ball milling process. It is noteworthy that the amount of hydrogen released for $LiAlH_4$-1 wt% NiCo@G reaches up to 7.3 wt%, which is identical to that of as-milled $LiAlH_4$. This phenomenon is attributed to the small NiCo@G percent and a good preservation of hydrogen during the ball milling process. Compared with the performance of other additives or catalysts, NiCo@G developed in this work exhibits high catalytic activity (Table S1†). For graphene, Hsu[29] and Jiang[36] suggested that the interaction between electronegative carbon and Li^+, high electronic conductivity promoting electron exchange between metal and $[AlH_4]^-$, and delocalized π bonds facilitates hydrogen release. Furthermore, in NiCo@G, graphene is the shell preventing NiCo nanoparticles aggregation, leading to NiCo nanoalloy with a uniform size distribution ranging from 4 to 6 nm. The beneficial effect of catalyst size on dehydrogenation behaviors has been confirmed in previous literatures.

Figure 3 shows the isothermal dehydrogenation kinetics measurements of as-milled $LiAlH_4$ and $LiAlH_4$-1 wt% NiCo@G at 150 °C. For as-milled $LiAlH_4$, only 1.6 wt% of hydrogen releases within 10 min. However, for-$LiAlH_4$-1 wt% NiCo@G, the dehydrogenation goes on rapidly with 5.8 wt% of hydrogen released within 10 min. Furthermore, total 7.3 wt% of hydrogen can be thoroughly released within 60 min for $LiAlH_4$-1 wt% NiCo@G while 350 min for as-milled $LiAlH_4$. This result confirms that dehydrogenation kinetics are significantly improved by addition of NiCo@G.

Dehydrogenation mechanism. To obtain insight on the catalytic mechanism of NiCo@G for the $LiAlH_4$ dehydrogenation, morphologies and intergrain dispersion of both as-milled $LiAlH_4$ and $LiAlH_4$-1 wt% NiCo@G are investigated by SEM, as shown in Fig. 4. Compared to as-milled $LiAlH_4$, the particle size significantly

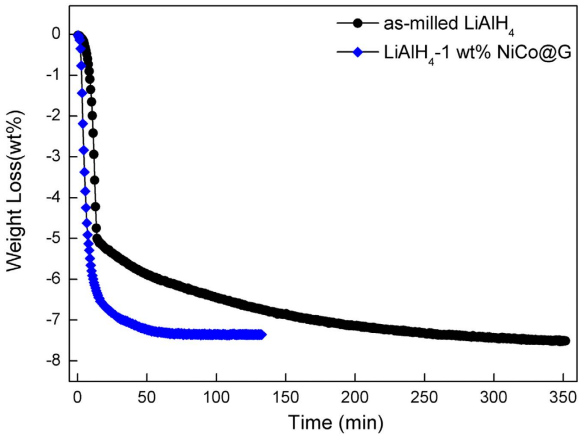

Figure 3. Isothermal dehydrogenation curves of as-milled $LiAlH_4$ and $LiAlH_4$-1 wt% NiCo@G at 150 °C.

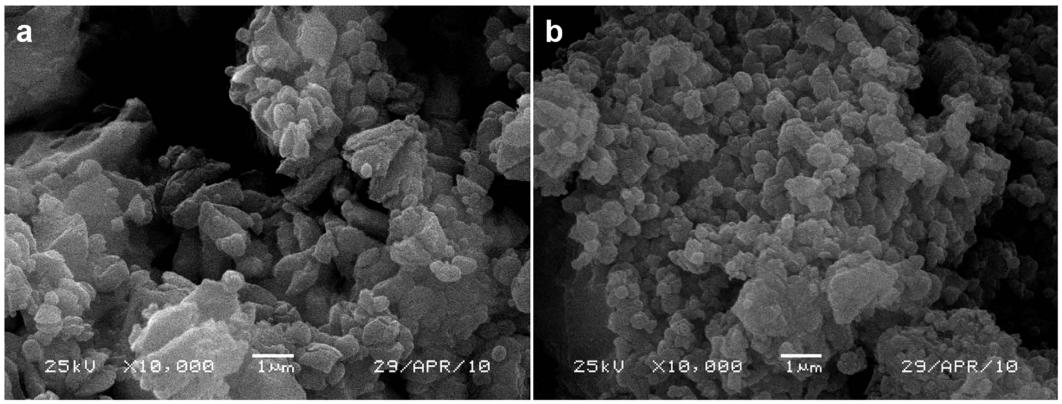

Figure 4. SEM images of: (**a**) as-milled $LiAlH_4$, (**b**) $LiAlH_4$-1 wt% NiCo@G.

decreases after doping with 1 wt% NiCo@G, leading to more grain boundaries and larger surface area. This important observation suggests that NiCo@G readily influences the $LiAlH_4$ texture at room temperature during the ball milling process, by preliminarily breaking their particle aggregation. Graphene has been confirmed as an effective grinding agent to reduce the crystal size of $LiAlH_4$ owing to its high mechanical strength[29,36]. At that stage it is not yet clear whether the consequent decrease of the dehydrogenation temperature is due to the smaller $LiAlH_4$ particles generated after ball milling or to another effect of the catalyst on the mechanism governing this decomposition. The strong catalytic effect of such a small percent of NiCo@G was further investigated by combining XRD and DSC.

Figure 5 shows the XRD patterns of NiCo@G, as-received $LiAlH_4$, as-milled $LiAlH_4$ and $LiAlH_4$-1 wt% NiCo@G. The diffraction peaks of as-milled $LiAlH_4$ match well with those of the as-received $LiAlH_4$, demonstrating a high stability of $LiAlH_4$ during the ball milling process. NiCo@G can not be distinguished in $LiAlH_4$-1 wt% NiCo@G, due to the exceptionally small concentration (1 wt%) of NiCo@G. The weak peaks of Li_3AlH_6 (2θ~21.9°, 31.6°) and Al (111) (2θ~38.4°) appear in $LiAlH_4$-1 wt% NiCo@G sample, indicating partial dehydrogenation of $LiAlH_4$ during ball milling process (R1), in agreement with the small hydrogen capacity loss observed in the TGA visualization of the dehydrogenation process (Fig. 2). Furthermore, the diffraction peaks of $LiAlH_4$ in the 1 wt% NiCo@G doped sample become broader than those of as-milled $LiAlH_4$, indicating smaller particle size of $LiAlH_4$.

DSC measurements were conducted to further verify the effect of NiCo@G on the dehydrogenation of $LiAlH_4$, as shown in Fig. 6a. Compared to as-received $LiAlH_4$, as-milled $LiAlH_4$ presents a similar DSC profile including the melting peak of $LiAlH_4$, indicating that the ball milling process does not alter its intrinsic properties. Surprisingly, the DSC profile of $LiAlH_4$-1 wt% NiCo@G is totally different and shows three distinct endothermic peaks. In order to understand the phase changes at different stages of $LiAlH_4$-1 wt% NiCo@G, we stopped the dehydrogenation of $LiAlH_4$-1 wt% at temperatures (110 °C, 170 °C and 210 °C) corresponding to three dehydrogenation stages in DSC profile and investigated the samples by XRD. As shown in Fig. 6b, Li_3AlH_6, Al and small amount of retained $LiAlH_4$ are present in the sample which was stopped dehydrogenation at 110 °C. Thus, the first endo peak in the DSC profile of $LiAlH_4$-1 wt% NiCo@G is attributed to the decomposition of solid $LiAlH_4$ (eqn.1). This decomposition (eqn. 1) apparently ends around 110 °C, which explains the absence of any $LiAlH_4$ melting. For the sample heated up to 170 °C corresponding to the second stage, Al, LiH, small amount of Li_3AlH_6

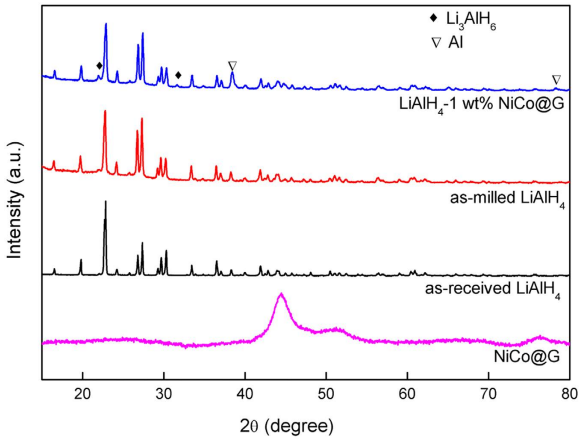

Figure 5. XRD patterns of NiCo@G, as-received $LiAlH_4$, as-milled $LiAlH_4$ and $LiAlH_4$-1 wt% NiCo@G.

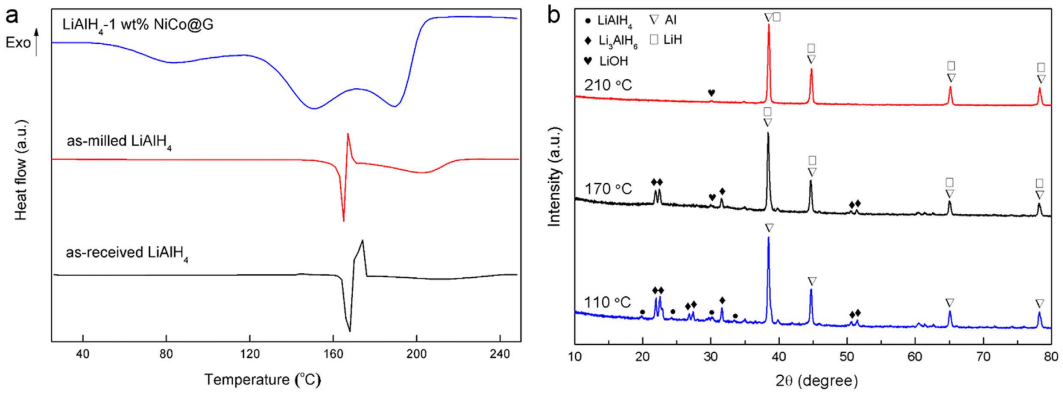

Figure 6. (**a**) DSC profiles of dehydrogenation of as-received $LiAlH_4$, as-milled $LiAlH_4$ and $LiAlH_4$-1 wt% NiCo@G at heating rate of 2 °C min^{-1}; (**b**) XRD patterns of $LiAlH_4$-1 wt% NiCo@G heated up to different temperatures (110 °C, 170 °C and 210 °C) corresponding to the DSC profile.

and LiOH are observed. Al, LiH and small amount of LiOH are present in the sample decomposed at 210 °C. So we can declare that the second and third peaks are attributed to the decomposition of solid Li_3AlH_6 (eqn. 2).

Activation energies. To understand the dehydrogenation kinetics, the apparent activation energy (E_a) at each stage of $LiAlH_4$-1 wt% NiCo@G dehydrogenation was calculated using the Kissinger equation (eqn. 3), considering the three endothermic peaks in DSC profiles at heating rates of 2, 5, 10 and 20 °C min^{-1}, as shown in Fig. 7.

$$\ln\left(\beta/T_p^{\,2}\right) = \ln(AR/E_a) - E_a/RT_p \tag{3}$$

where β is the heating rate, T_p (K) is the DSC peak temperature, A is the pre-exponential factor, and R is the gas constant. E_a, for each dehydrogenation stage of $LiAlH_4$-1 wt% NiCo@G, was evaluated to be 54.8 ± 6 kJ mol^{-1}, 80.1 ± 1.3 kJ mol^{-1} and 119.7 ± 2.8 kJ mol^{-1} respectively. The activation energy E_{a1} for R1 involved in the catalytic dehydrogenation of $LiAlH_4$ is comparable to the lowest values of those reported catalysts.

Regarding the superior efficiency of NiCo@G, many factors obviously play a role. Such efficiency can either be attributed to the support (carbon)[29] or to a combination of properties associated with two different nanosized metals[37,38] or to both[19,39,40]. The mechanism need further investigations for the particular NiCo bimetallic nanoparticles encapsulated in graphene used here.

As a summary, NiCo nanoalloy (4–6 nm) encapsulated in grapheme layers (NiCo@G) was prepared and introduced into $LiAlH_4$ by solid-state ball milling. A tremendous improvement in the dehydrogenation properties of $LiAlH_4$ was achieved. When 1 wt% NiCo@G was doped with $LiAlH_4$, the onset dehydrogenation temperature is decreased to 43 °C with 7.3 wt% of hydrogen released below 200 °C. For $LiAlH_4$ doped with 10 wt% NiCo@G, the onset dehydrogenation temperature is as low as 36 °C, which is 116 °C lower than that of pristine $LiAlH_4$. Ea of $LiAlH_4$-1 wt% NiCo@G for the first dehydrogenation step decreased to 54.8 kJ mol^{-1}. The significant catalytic effect makes NiCo@G a promising candidate for $LiAlH_4$ dehydrogenation. A more in depth study of the effect of NiCo@G on $LiAlH_4$ dehydrogenation, in particular regarding the critical roles of Ni/Co and catalyst/$LiAlH_4$ ratios, is in process.

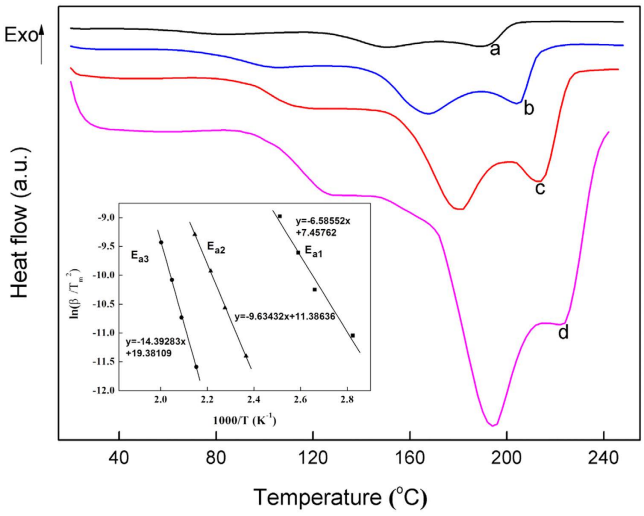

Figure 7. DSC profiles of $LiAlH_4$-1 wt% NiCo@G at heating rates of 2 (**a**), 5 (**b**), 10 (**c**) and 20 °C min^{-1} (**d**). The inset graph is Kissinger plots for the three stages of dehydrogenation of $LiAlH_4$-1 wt% NiCo@G.

Methods

Chemicals. All reagents and chemicals were commercially available and of analytical grade without further purification prior to use, unless specifically stated elsewhere.

Preparationof NiCo@G. The precursor complex $CoCo[Ni(EDTA)]_2{\cdot}4H_2O$ was synthesized by solvothermal method as reported previously[30]. Pyrolysis of $CoCo[Ni(EDTA)]_2{\cdot}4H_2O$ was performed under an argon (99.999%) flow at 500 °C for 3 h. The final sample was denoted as NiCo@G.

Preparation of $LiAlH_4$-NiCo@G samples. $LiAlH_4$ (97%) was purchased from Alfa Aesar, and used without further purification. Typically, 0.5 g powder mixture composed of $LiAlH_4$ and NiCo@G was loaded into a stainless milling pot with 10 steel balls (10 mm in diameter). Ball milling was carried out on a QM-1SP2 planetary under an argon atmosphere at 300 rpm for 30 min. All sample handlings were performed in a glove box filled with argon to avoid oxidation and moisture.

Characterizations. Powder X-ray diffraction (XRD) measurements were conducted on a PANalytical X'pert diffractometer operated at 40 kV and 40 mA with a Cu K_α radiation ($\lambda = 1.5418$ nm). The samples were covered by Mylar film in glove box to avoid oxidation and moisture. Scanning electron microscopy (SEM) images were obtained by using JSM-6360LV SEM (JEOL, Japan). Transmission electron microscopy (TEM) studies were performed on a FEI Tecnai F30 microscope and a G^2 microscope operated at 300 kV. The powders were dropped on an ultrathin carbon film supported on a copper grid by using ethanol as a dispersant. X-ray photoelectron spectroscopy (XPS) was recorded using a Thermo ESCALAB 250Xi instrument with Al Kα X-rays (1486.6 eV). Thermogravimetric analysis (TGA) was carried out on a Cahn Thermax 500 with a heating rate of 2 °C min^{-1} in an argon flow. The isothermal dehydrogenation kinetics were measured using a Sieverts-type apparatus (Advanced Materials Corporation, USA) at 150 °C under an initial pressure of 10^{-5} MPa. Differential scanning calorimetry (DSC) data was collected from a TA Q1000 in a constant argon flow (50 mL min^{-1}) at different heating rates (2 K min^{-1}, 5 K min^{-1},10 K min^{-1}, 20 K min^{-1}).

References

1. Sevilla, M. & Mokaya, R. Energy storage applications of activated carbons: supercapacitors and hydrogen storage. *Energy Environ. Sci.* **7,** 1250–1280 (2014).
2. Wang, W. & Yuan, D. Mesoporous carbon originated from non-permanent porous MOFs for gas storage and CO_2/CH_4 separation. *Sci. Rep.* **4,** 5711; doi: 10.1038/srep05711 (2014).
3. Sung Cho, H. *et al.* Extra adsorption and adsorbate superlattice formation in metal-organic frameworks. *Nature.* **527,** 503–507 (2015).
4. Murray, L. J., Dinca, M. & Long, J. R. Hydrogen storage in metal-organic frameworks. *Chem. Soc. Rev.* **38,** 1294–1314 (2009).
5. Lai, Q. *et al.* Hydrogen storage materials for mobile and stationary applications: current state of the art. *Chemsuschem.* **8,** 2789–2825 (2015).
6. Zhang, L. *et al.* Remarkably improved hydrogen storage performance of MgH_2 catalyzed by multivalence NbH_x nanoparticles. *J. Phys. Chem. C.* **119,** 8554–8562 (2015).
7. Balde, C. P., Hereijgers, B. P. C., Bitter, J. H. & de Jong, K. P. Facilitated hydrogen storage in $NaAlH_4$ supported on carbon nanoribers. *Angew. Chem. Int. Ed.* **45,** 3501–3503 (2006).
8. Staubitz, A., Robertson, A. P. M. & Manners, I. Ammonia-Borane and related compounds as dihydrogen sources. *Chem. Rev.* **110,** 4079–4124 (2010).
9. Yao, Q., Lu, Z. H., Yang, K., Chen, X. & Zhu, M. Ruthenium nanoparticles confined in SBA-15 as highly efficient catalyst for hydrolytic dehydrogenation of ammonia borane and hydrazine borane. *Sci. Rep.* **5** (2015).
10. Schlapbach, L. & Zuttel, A. Hydrogen-storage materials for mobile applications. *Nature.* **414,** 353–358 (2001).

11. Liu, S. S. *et al.* Effect of ball milling time on the hydrogen storage properties of TiF_3-doped $LiAlH_4$. *Int. J. Hydrogen Energy.* **34,** 8079–8085 (2009).
12. Liu, Y., Hu, J., Wu, G., Xiong, Z. & Chen, P. Large amount of hydrogen desorption from the mixture of $Mg(NH_2)_{(2)}$ and $LiAlH_4$. *J. Phys. Chem. C.* **111,** 19161–19164 (2007).
13. Liu, X. *et al.* Ti-doped $LiAlH_4$ for hydrogen storage: synthesis, catalyst loading and cycling performance. *J. Am. Chem. Soc.* **133,** 15593–15597 (2011).
14. Li, Z. *et al.* Enhanced hydrogen storage properties of $LiAlH_4$ catalyzed by $CoFe_2O_4$ nanoparticles. RSC *Adv.* **4,** 18989–18997 (2014).
15. Liu, X., McGrady, G. S., Langmi, H. W. & Jensen, C. M. Facile cycling of Ti-doped $LiAlH_4$ for high performance hydrogen storage. *J. Am. Chem. Soc.* **131,** 5032–5033 (2009).
16. Varin, R. A. & Parviz, R. The effects of the micrometric and nanometric iron (Fe) additives on the mechanical and thermal dehydrogenation of lithium alanate ($LiAlH_4$), its self-discharge at low temperatures and rehydrogenation. *Int. J. Hydrogen Energy.* **37,** 9088–9102 (2012).
17. Resan, M., Hampton, M. D., Lomness, J. K. & Slattery, D. K. Effects of various catalysts on hydrogen release and uptake characteristics of $LiAlH_4$. *Int. J. Hydrogen Energy.* **30,** 1413–1416 (2005).
18. Li, P. *et al.* $NiFe_2O_4$ nanoparticles catalytic effects of improving $LiAlH_4$ dehydrogenation properties. *J. Phys. Chem. C.* **117,** 25917–25925 (2013).
19. Tan, C. Y. & Tsai, W. T. Catalytic and inhibitive effects of Pd and Pt decorated MWCHTs on the dehydrogenation behavior of $LiAlH_4$. *Int. J. Hydrogen Energy.* **40,** 10185–10193 (2015).
20. Zheng, X., Qu, X., Humail, I. S., Li, P. & Wang, G. Effects of various catalysts and heating rates on hydrogen release from lithium alanate. *Int. J. Hydrogen Energy.* **32,** 1141–1144 (2007).
21. Li, L. *et al.* Enhancement of the H_2 desorption properties of $LiAlH_4$ doping with $NiCo_2O_4$ nanorods. *Int. J. Hydrogen Energy.* **39,** 4414–4420 (2014).
22. Tan, C. Y. & Tsai, W. T. Effects of Ni and Co-decorated MWCNTs addition on the dehydrogenation behavior and stability of $LiAlH_4$. *Int. J. Hydrogen Energy.* **40,** 14064–14071 (2015).
23. Li, L., Wang, Y., Jiao, L. & Yuan, H. Enhanced catalytic effects of Co@C additive on dehydrogenation properties of $LiAlH_4$. *J. Alloys Compd.* **645,** S468–S471 (2015).
24. Wahab, M. A. & Beltramini, J. N. Catalytic nanoconfinement effect of in-situ synthesized Ni-containing mesoporous carbon scaffold (Ni-MCS) on the hydrogen storage properties of $LiAlH_4$. *Int. J. Hydrogen Energy.* **39,** 18280–18290 (2014).
25. Shan, S. *et al.* Atomic-structural synergy for catalytic CO oxidation over palladium-nickel nanoalloys. *J. Am. Chem. Soc.* **136,** 7140–7151 (2014).
26. Prieto, G. *et al.* Design and synthesis of copper-cobalt catalysts for the selective conversion of synthesis gas to ethanol and higher alcohols. *Angew. Chem. Int. Ed.* **53,** 6397–6401 (2014).
27. Garcia, S., Zhang, L., Piburn, G. W., Henkelman, G. & Humphrey, S. M. Microwave synthesis of classically immiscible rhodium-silver and rhodium-gold alloy nanoparticles: highly active hydrogenation catalysts. *Acs Nano.* **8,** 11512–11521 (2014).
28. Niu, W., Gao, Y., Zhang, W., Yan, N. & Lu, X. Pd-Pb alloy nanocrystals with tailored composition for semihydrogenation: taking advantage of catalyst poisoning. *Angew. Chem. Int. Ed.* **54,** 8271–8274 (2015).
29. Hsu, C. P. *et al.* Buckyball-, carbon nanotube-, graphite-, and graphene-enhanced dehydrogenation of lithium aluminum hydride. *Chem. Commun.* **49,** 8845–8847 (2013).
30. Sapina, F., Coronado, E., Beltran, D. & Burriel, R. From 1-D to 3-D ferrimagnets in the EDTA family–magnetic characterization of the tetrahydrate series$MtM(M'EDTA)_2$.cntdot.$4H_2O$ [Mt, M, M' = cobalt(II), nickel(II), zinc(II)]. *J. Am. Chem. Soc.* **113,** 7940–7944 (1991).
31. Chen, L., Zhu, Q. & Wu, R. Effect of Co-Ni ratio on the activity and stability of Co-Ni bimetallic aerogel catalyst for methane Oxy-CO_2 reforming. *Int. J. Hydrogen Energy.* **36,** 2128–2136 (2011).
32. Rashid, M. H., Raula, M. & Mandal, T. K. Polymer assisted synthesis of chain-like cobalt-nickel alloy nanostructures: magnetically recoverable and reusable catalysts with high activities. *J. Mater. Chem.* **21,** 4904–4917 (2011).
33. Zhang, G., Sun, S., Bostetter, M., Poulin, S. & Sacher, E. Chemical and morphological characterizations of CoNi alloy nanoparticles formed by co-evaporation onto highly oriented pyrolytic graphite. *J. Colloid Interface Sci.* **350,** 16–21 (2010).
34. Majumdar, D., Spahn, R. G. & Gau, J. S. X-Ray Photoelectron-spectroscopy studiesontheoxidation behavior of CoNi thin films. *J. Electrochem. Soc.* **134,** 1825–1829 (1987).
35. Singh, S. K., Singh, A. K., Aranishi, K. & Xu, Q. Noble-metal-free bimetallic nanoparticle-catalyzed selective hydrogen generation from hydrous hydrazine for chemical hydrogen storage. *J. Am. Chem. Soc.* **133,** 19638–19641 (2011).
36. Jiang, D. H., Yang, C. H., Tseng, C. M., Lee, S. L. & Chang, J. K. Metal/graphene nanocomposites synthesized with the aid of supercritical fluid for promoting hydrogen release from complex hydrides. *Nanoscale.* **6,** 12565–12572 (2014).
37. Ferrando, R., Jellinek, J. & Johnston, R. L. Nanoalloys: from theory to applications of alloy clusters and nanoparticles. *Chem. Rev.* **108,** 845–910 (2008).
38. Wang, D. & Li, Y. Bimetallic nanocrystals: liquid-phase synthesis and catalytic applications. *Adv. Mater.* **23,** 1044–1060 (2011).
39. Tavakkoli, M. *et al.* Single-shell carbon-encapsulated iron nanoparticles: synthesis and high electrocatalytic activity for hydrogen evolution reaction. *Angew. Chem. Int. Ed.* **54,** 4535–4538 (2015).
40. Tan, C. Y. & Tsai, W. T. Effects of $TiCl_3$-decorated MWCNTs addition on the dehydrogenation behavior and stability of $LiAlH_4$. *Int. J. Hydrogen Energy.* **39,** 20038–20044 (2014).

Acknowledgements

The authors wish to acknowledge the financial support from the National Natural Science Foundation of China (21403267, 21373215, 51361005, U1501242, 21173111, 51371060, 51201042, 51461010 and 51201041), Shandong Postdoctoral Innovation Program (201303065) and Guangxi Natural Science Foundation (2014jjDA20005, 2014jjAA60035), Guangxi Key Laboratory of Information Materials (1210908–217-Z) and Guangxi Scientific Technology Team (2012GXNSFGA06002, 2015GXNSFFA139002).

Author Contributions

L.X.S. directed the project and designed the experimental scheme. C.L.J. performed experiments and wrote the paper. F.X. revised the manuscript. S.S.L. analyzed the dehydrogenation mechanism. J.Z. analyzed the dehydrogenation performances. X.J. analyzed the activation energies. L.N.Y. helped with the experiment.

Additional Information

Supplementary information accompanies this paper at http://www.nature.com/srep

Competing financial interests: The authors declare no competing financial interests.

How to cite this article: Jiao, C. *et al.* NiCo nanoalloy encapsulated in graphene layers for improving hydrogen storage properties of $LiAlH_4$. *Sci. Rep.* **6**, 27429; doi: 10.1038/srep27429 (2016).